A Journal of the Gesellschaft Deutscher Chemiker
Angewandte Chemie
International Edition
www.angewandte.org

**Title:** A Janus Fe-SnO2 Catalyst Enables Bifunctional Electrochemical Nitrogen Fixation

**Authors:** Linlin Zhang, Meiyu Cong, Xin Ding, Yu Jin, Fanfan Xu, Yong Wang, Lin Chen, and Lixue Zhang

**To be cited as:** *Angew. Chem. Int. Ed.* 10.1002/anie.202003518

**Link to VoR:** https://doi.org/10.1002/anie.202003518

WILEY-VCH

Angewandte Chemie International Edition 10.1002/anie.202003518

# A Janus Fe-$SnO_2$ Catalyst Enables Bifunctional Electrochemical Nitrogen Fixation

Linlin Zhang [a], Meiyu Cong [a], Xin Ding [a,b]*, Yu Jin [b], Fanfan Xu [a],Yong Wang [c], Lin Chen [d], Lixue Zhang [a] *

Dedication ((optional))

**Abstract:** Electrochemical $N_2$ reduction reactions (NRR) and $N_2$ oxidation reaction (NOR), using $H_2O$ and $N_2$, represent a sustainable approach to $N_2$ fixation and arouse widespread attention. To date, due to the chemical inertness of nitrogen, emerging electrocatalysts for the electrochemical NRR and NOR at room temperature and atmospheric pressure remain largely under explored. Herein, a new-type Fe–$SnO_2$ was rationally designed as a Janus electrocatalyst for achieving highly efficient NRR and NOR catalysis. A high $NH_3$ yield of 82.7 μg $h^{-1}$ $mg_{cat.}^{-1}$ and a Faraday efficiency (FE) of 20.4 % were obtained for NRR, superior than all noble-metal-free electrocatalysts reported in acid electrolyte. This catalyst can also serve as an excellent NOR electrocatalyst with a $NO_3^-$ yields of 42.9 μg $h^{-1}$ $mg_{cat.}^{-1}$ and a FE of 0.84%. By means of experiments and density functional theory (DFT) calculations, we reveal that the oxygen vacancy-anchored single-atom Fe can effectively adsorb and activate chemical inert $N_2$ molecules, lower the energy barrier for the vital breakage of N≡N, resulting in the enhanced $N_2$ fixation performance.

Nitrogen is indispensable in the biosynthesis of the basic building-block molecules that sustain all forms of life, e.g., amino acids and nucleotides that constitute DNA/RNA.[1, 2] The usual fixed-nitrogen compounds are $NH_3$ and $HNO_3$, which are formed in nature by biological nitrogenases and lightning. The worldwide production of $NH_3$ and $HNO_3$ was 150 and 50 million metric tons, respectively, in 2017. In industry, $NH_3$ is synthesized by the Haber–Bosch process, which involves reacting $H_2$ and $N_2$ at high temperature (400–500 °C) and high pressure (20–30 MPa).[3-5] The commercial $HNO_3$ was produced through the catalytic oxidation of $NH_3$ (Ostwald process), followed by a multistep chemical reaction under harsh reaction conditions (15–25 MPa, 400–600°C).[6-8] These processes are both energy intensive, consuming tremendous global power and discharging global greenhouse gas. Developing a more efficient and environmentally friendly alternative technique for $N_2$ fixation is therefore desirable from both energy and environment needs. Advanced electrocatalysts for electrochemical $N_2$ reduction reactions (NRR) and $N_2$ oxidation reaction (NOR), represent a sustainable approach to $N_2$ fixation and arouse widespread attention. An effective $N_2$ fixation electrocatalyst should possess sufficient active sites and in particular optimized electron structure that can selectively absorb and activate the chemically inert $N_2$ and effectively suppress the side reactions during $N_2$ fixation, *i.e.* hydrogen evolution reaction (HER) during NRR or oxygen evolution reaction (OER) during NOR.[9-23]

Taking into account its thermal stability, acid resistance and inactivity toward both HER and OER,[24-26] $SnO_2$ was regarded as a promising catalyst candidate for $N_2$ fixation. Unfortunately, the reported $SnO_2$ catalysts still showed the limited catalytic activity for NRR mainly because they had relatively low conductivity, poor adsorption and weak activation for $N_2$.[27,28] Herein, we bypass these obstacles to $N_2$ fixation by designing a new-type Fe–$SnO_2$ catalyst, inspired by the natural phenomenon that Fe, as one of the cheapest and most abundant metals on the earth, exists in biological nitrogenases for natural $N_2$ fixation.[29,30] Different from the previously reported nanostructured Fe-based NRR catalysts,[31-37] the Fe–$SnO_2$ catalyst presents a unique surface structure. The Fe elements in Fe–$SnO_2$ can be categorized into oxygen vacancy-anchored single-atom Fe and lattice doped Fe, which are new strategies for enhancing the adsorption and activation of $N_2$ on $SnO_2$ and improving the electrical conductivity of $SnO_2$, respectively. The out-bond activation abilities of Fe–$SnO_2$ largely lowered the energy barrier for the vital breakage of chemical inert $N_2$ molecule. As a consequence, the designed Fe–$SnO_2$ catalyst exhibited excellent bifunctional catalytic performance toward both NRR and NOR: a high $NH_3$ yield of 82.7 μg $h^{-1}$ $mg_{cat.}^{-1}$ and a Faraday efficiency (FE) of 20.4% for the NRR, as the most active noble-metal-free electrocatalysts in acid electrolyte,[38-43] and a high $NO_3^-$ yields of 42.9 μg $h^{-1}$ $mg_{cat.}^{-1}$ and a FE of 0.84% for NOR in 0.05 M $H_2SO_4$.

This Fe–$SnO_2$ catalyst was prepared by a simple hydrothermal reaction (see details in Supporting Information). Figure 1A shows that the X-ray diffraction (XRD) patterns of $SnO_2$ doped with different proportions of Fe displayed seven peaks, at 26.61º, 33.89º, 37.95º, 51.78º, 57.81º, 65.91º, and 71.27º, corresponding to the (110), (101), (200), (211), (002), (301), and (202) planes, respectively, of $SnO_2$ (JCPDS No. 41-1445). Neither iron oxide nor hydroxide was detected in the XRD pattern. The chemical compositions and binding states of Fe–$SnO_2$ were investigated by X-ray photoelectron spectroscopy (XPS; Figure 1B and S1). The Sn 3d XPS spectra showed two peaks, at 486.4 and 494.2 eV, which can be assigned to $3d_{5/2}$ and $3d_{3/2}$. A positive shift of the $SnO_2$ binding energy was

---

[a] L. Zhang, M. Cong, X. Ding, F. Xu, L. Zhang
College of Chemistry and Chemical Engineering
Institution Qingdao University
Qingdao 266071, Shandong, PR China
E-mail: dingxin@qdu.edu.cn; zhanglx@qdu.edu.cn
[b] X. Ding, Y. Jin
State Key Laboratory of Fine Chemicals, Dalian University of Technology (DUT), Dalian 116024, Liaoning, PR China
[c] Y. Wang
Technische Universität München Department Chemie Lichtenbergstr. 4 D-85748 Garching Germany
[d] L. Chen,
State Key Laboratory of Environment-friendly Energy Materials, Southwest University of Science and Techaology, Mianyang 621010, Sichuan PR China.

Supporting information for this article is given via a link at the end of the document. ((Please delete this text if not appropriate)) observed in the Sn 3d XPS spectrum after Fe doping, indicative for the reduced nature of oxygen vacancy on Fe-$SnO_2$ surface. Doping with Fe was confirmed by the Fe 3p spectrum of Fe–$SnO_2$. The Fe 3p spectra showed two peaks, at 56.4 and 59.7 eV, corresponding to $3p_{3/2}$ and $3p_{1/2}$, respectively; and the peak intensities increased with increasing dopant from 0% to 7%.

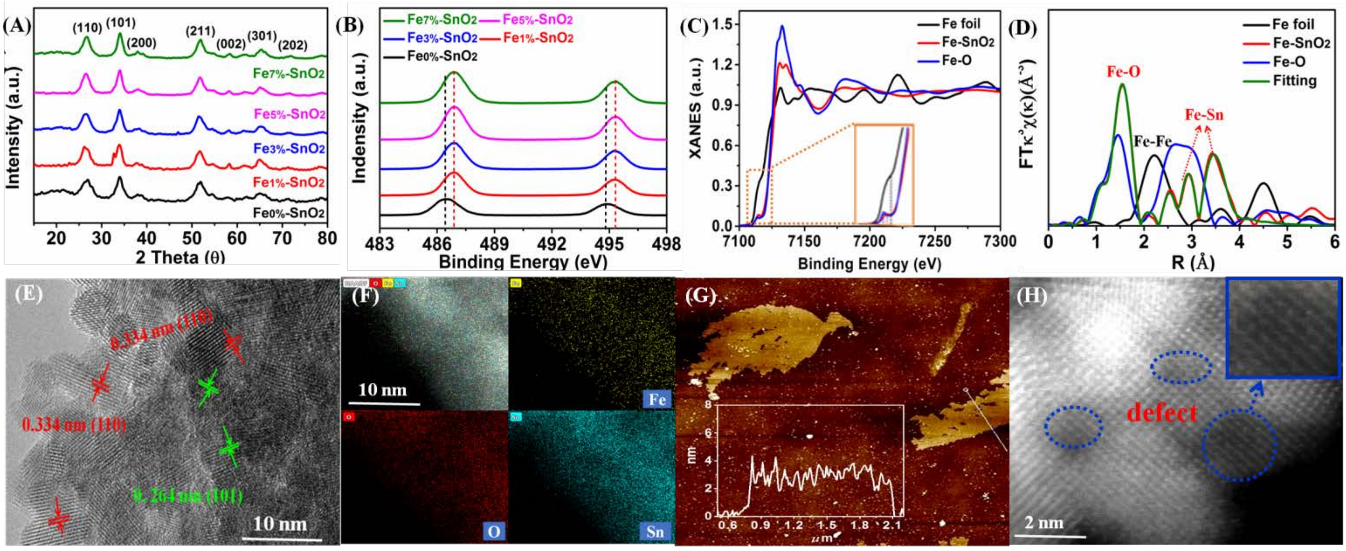

**Scheme 1.** (A) XRD patterns of catalysts, (B) XPS survey spectra of catalysts, (C) Fe K-edge XANES spectra of Fe–$SnO_2$, $Fe_2O_3$, and Fe foil, (D) Fourier transforms of k3-weighted Fe K-edge of EXAFS spectra of Fe–$SnO_2$, $Fe_2O_3$, and Fe foil; (E) HR-TEM image of Fe–$SnO_2$, (F) EDS elemental mapping images of Fe, Sn, and O in Fe–$SnO_2$, (G) AFM image and corresponding line profiles, and (H) HAADF-STEM image of Fe–$SnO_2$

Previously, the roles of oxygen vacancies in heteroatoms doped transition metal oxides have been extensively discussed, and the low-valance dopants have been shown to facilitate the formation of oxygen vacancies.[44-46] Herein, the oxygen vacancy was studied with XPS and Electron paramagnetic resonance (EPR). The O 1s XPS patterns shows three main peaks at 529.9, 531.1, and 531.9 eV (Figure S2), which belong to the lattice oxygen, oxygen atoms in vicinity of oxygen vacancy and chemisorbed oxygen, respectively.[44] The distinct EPR signals at g = 2.004, from the electrons trapped in oxygen vacancy, show that a large amount of oxygen vacancies generated on both $SnO_2$ and Fe-$SnO_2$ samples (Figure S3). Interestingly, the peak intensities in the O 1s XPS and EPR spectra clearly decreased after Fe doping. These observations suggest the possible formation of oxygen vacancy-anchored Fe. Similar to the previous work by Wan *et al*, the oxygen vacancies formed on ultrathin $SnO_2$ can serve as “traps” to capture iron ion in acid solution and anchor Fe atoms.[45-46] This deduction was also in agreement with the positive shift in Sn 3d XPS spectra in Figure 1(B). Then, the states of Fe element in Fe–$SnO_2$ were further identified by Fe K-edge X-ray absorption near-edge structure (XANES) spectroscopy. The XANES spectra of Fe–$SnO_2$, standard $Fe_2O_3$ (Fe–O), and Fe foil are shown in Figure 1C. The near-edge of Fe–$SnO_2$ is found to be between those of Fe foil and $Fe_2O_3$, suggesting that the average valence state of Fe is between $Fe^0$ and $Fe^{III}$. The Fe chemical environment was then probed by extended X-ray absorption fine structure (EXAFS) spectroscopy (Figure 1 D, Figure S4-S5, and Table S1). The EXAFS results show that there is no first-shell Fe–Fe contribution for the Fe–$SnO_2$ sample, which suggests that the major Fe species are not in the form of metallic Fe nanoparticles or clusters. Instead, Fe–$SnO_2$ gives a first-shell Fe–O contribution with a coordination number of about 3.6 at 2.01 Å, and a first-shell Fe–Sn contribution with a coordination number of about 0.4 at 3.12 Å, which can be assigned to lattice doped Fe. The first-shell Fe–Sn contribution with a coordination number of about 4.4 at 3.87 Å can be assigned to Fe anchored at oxygen vacancies, forming Sn-Fe-Sn structure.[47-50] Therefore, the Fe elements in Fe–$SnO_2$ can therefore be categorized into isolated single-atom Fe confined distribution on surface with oxygen vacancies and lattice doped Fe.

The morphologies and structures of nanosized Fe–$SnO_2$ catalyts were investigated by high-resolution transmission electron microscopy (HR-TEM; Figure 1E) and atomic force microscopy (AFM; Figure 1G). Fe–$SnO_2$ shows two characteristic spacing of 0.334 and 0.264 nm for the (110) and (101) lattice planes, respectively. Energy-dispersive spectroscopy (EDS) mapping showed that Fe, Sn, and O elements were homogeneously distributed in Fe–$SnO_2$. The AFM images showed two-dimensional Fe–$SnO_2$ possessed a thickness *ca.*3 nm. Local defects were obtained after Fe doping from the atomic arrangement in atomic-level high-angle annular dark field-scanning TEM (HAADF-STEM) images (Figure 1H and Figure S6)

The electrochemical $N_2$ reduction was performed in an H-type cell with pretreated 0.1 M HCl electrolyte. An Ag/AgCl reference electrode was placed in the cathode chamber. The counter electrode, which was in the anode chamber, was a graphite plate. Before the tests, the pretreated $N_2$ was bubbled into the cathode chamber, rather than continuous flow of $N_2$. Protons were transported through the electrolyte and reacted with $N_2$ on the catalyst surface to produce $NH_3$. The $NH_3$ yield

10.1002/anie.202003518
WILEY-VCH

was calculated by UV-vis absorption spectroscopy (Figure S7) and ion chromatography (Figure S8-S9). The polarization curves of Fe-$SnO_2$ ($Fe_{3\%}$-$SnO_2$, if without special instructions) from LSV measurements were shown in Figure 2A. The potential range could be divided into NRR favorable region (ranging from -0.2 V to -0.5 V vs RHE) and HER favorable region (lower than -0.5 V vs RHE). In the NRR region, the current density in $N_2$ saturated electrolyte was much higher than that in Ar saturated electrolyte for the contribution of NRR. The chronoamperometry curves for Fe–$SnO_2$ at various potentials in NRR favorable range are shown in Figure 2B. The current density increased with the potential. After 2 h of the electrocatalytic reaction, the $NH_3$ yield and FE obtained for the NRR reached maximum values at an applied potential of −0.3 V with a high $NH_3$ yield of 82.7 μg $h^{-1}$ $mg_{cat.}^{-1}$ and a high FE of 20.4% (Figure 2C and Figure S10-11), which is superior than all noble-metal-free electrocatalysts reported in acid electrolyte. The amount of $N_2H_4$ as a byproduct was determined by the Watt−Chrisp method (Figure S12).[5] Figure S13 shows the UV-vis absorption spectra of the electrolytes stained with *p*-$C_9H_{11}NO$ indicator after NRR electrolysis at different potentials. The absence of $N_2H_4$ indicates that the reaction on Fe–$SnO_2$ gives excellent selectivity for $NH_3$ production. Stability tests showed minimal changes in the $NH_3$ yield (calculated from ion chromatograms and UV-vis absorption spectra) over five reaction cycles (Figure S14-17). The FE remained at ~20%, which indicates that Fe–$SnO_2$ displays high stability in the NRR. The stability could be further confirmed from the long-time operation as shown in Figure S18. As shown in Figure S19-21, comparison experiments show that the Fe-$SnO_2$ displays a much more enhanced NRR activity than commercially available routine $SnO_2$ and the vacancy-rich $SnO_2$ (i.e. $Fe_{0\%}$-$SnO_2$), which should be due to the unique Fe dopant as surface defective active sites. The doping amount of Fe affected the catalytic activity, and the maximum $NH_3$ yield and FE were obtained when the Fe ratio was 3% (Figure S22-25). Additionally, the isotope labeling experiments were carried out in a simple and economic pahtway as shown in supporting information, in a $^{15}N_2$-saturated electrolyte experiment, $^{15}NH_4^+$ with a specific double peak was detected (Figure 2D). These results suggest that the detected $NH_3$ was completely derived from the electrochemical reduction of $N_2$, rather than from $NH_3$ or $NO_3^-$ contaminants..

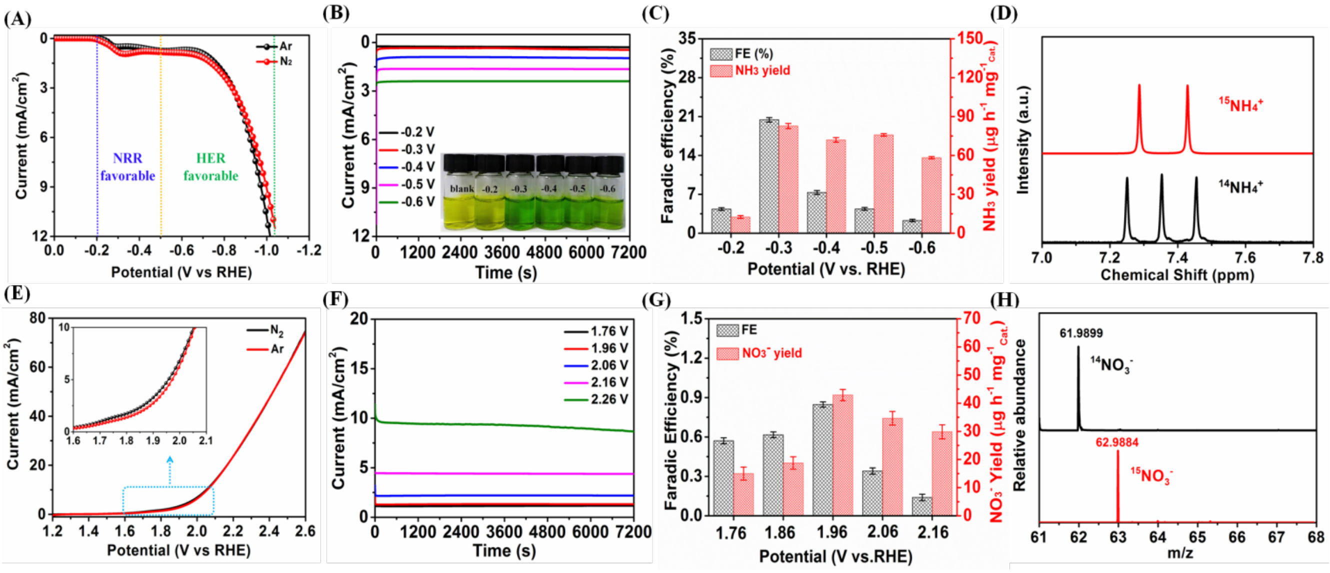

**Figure 2.** (A) LSV curves for Fe–$SnO_2$ under Ar saturated and $N_2$ saturated electrolyte; (B) Dependence of current density on time for NRR with Fe–$SnO_2$ as catalyst at various applied potentials(insert: the photograph of electrolyte treated using a indophenol blue method); (C) FEs and $NH_3$ production for NRR with Fe–$SnO_2$ at various applied potentials; (D) $^1H$ NMR spectra of both $^{14}NH_4^+$ and $^{15}NH_4^+$ produced from the NRR tests (at -0.3 V vs. RHE) using $^{14}N_2$ or $^{15}N_2$ as $N_2$ source; (E) LSV curves for Fe -$SnO_2$ under Ar saturated and $N_2$ saturated electrolyte; (F) Dependence of current density on time for NOR with Fe–$SnO_2$ as catalyst at various applied potentials; (G) FE and $NO_3^-$ production for NOR with Fe–$SnO_2$ at various applied potentials; (E) FEs and yield rates in Fe–$SnO_2$ cycling tests; (H) MS spectra of both $^{14}NO_3^-$ and $^{15}NO_3^-$ produced from the NOR tests (at 1.96 V vs. RHE) using $^{14}N_2$ or $^{15}N_2$ as $N_2$ source.

Electrochemical NOR tests were performed in the same electrolytic cell with pretreated 0.05 M $H_2SO_4$ electrolyte. $N_2$ reacted with $H_2O$ on the catalyst surface to produce $NO_3^-$. The $NO_3^-$ yield was calculated by ion chromatography (Figure S26-27). The LSV polarization curves of Fe-$SnO_2$ were shown in Figure 3 E. The faradic range for NOR started from 1.6 V to 2.1 V vs RHE for Fe-$SnO_2$. As shown in the chronoamperometry curves for Fe–$SnO_2$ at various potentials (Figure 3F), the current density increased with increasing potential from 1.76 to 2.16 V. After 2 h of the electrocatalytic reaction, a high $NO_3^-$ yield of 42.9 μg $h^{-1}$ $mg_{cat.}^{-1}$ and a high FE of 0.84% were obtained for NOR at an applied potential of 1.96 V (Figure 2G, Figure S28). Stability tests show minimal changes in the $NO_3^-$ yield over five reaction cycles and in the current density of long-time operation (Figure S29-32), indicating that Fe–$SnO_2$ has high stability in the NOR. The results show that the maximum $NO_3^-$ yield and FE were also obtained at a Fe ratio of 3% (Figure S33-35). The isotope labeling experiments were performed to verify that the detected $NO_3^-$ was generated via the NOR process (Figure S36 and Figure 2H). In the $^{15}N_2$-saturated electrolyte experiment, $^{15}NO_3^-$ was obtained with a molecular weight of 62.9884, compared with that of 61.988 for $^{14}NO_3^-$ in the $^{14}N_2$-saturated electrolyte. Additionally, no $NO_3^-$ was detected under open-circuit conditions and in an Ar-saturated electrolyte after electrolysis for 2 h. These results suggest that the detected $NO_3^-$ was completely derived from the electrochemical oxidation of $N_2$.

DFT simulations were performed to investigate the bonding nature of the active centers and energetic pathways of $N_2$ reduction and oxidation over Fe-$SnO_2$(110) catalysts under acidic conditions (Figure 3A-B, S37 and Table S2). As shown, $N_2$ molecules interact weakly with the $SnO_2$(110) surface ($\Delta G_{N2}$: 0.337 eV), vacancy-rich $SnO_2$(110) surface ($\Delta G_{N2}$: 0.05 eV), lattice doped Fe in Fe–$SnO_2$ ($\Delta G_{N2}$: 0.41 eV for Fe site, -0.04 eV for single/bi-Sn site) and the single/bi-Sn site in Fe–$SnO_2$ with surface-anchored Fe ($\Delta G_{N2}$: 0.50 eV). The oxygen vacancy-anchored Fe, which probably exists as protrusion-shaped isolated active site, can effectively adsorb and activate $N_2$ molecules, as reflected by the favorable $N_2$ adsorption free energy (−0.49 eV) and an increased N≡N bond length (1.136 Å). Therefore, the oxygen vacancy-anchored Fe should be the active sites in Fe–$SnO_2$, rather than the single Sn or the newly proposed adjacent bi-Sn ion pairs.[9,10,51]

The NRR kinetic pathway was then investigated based on the calculated Gibbs free energy (ΔG) diagrams. Theoretically, the associative distal pathway has been proved to be more energetically preferable over an alternating pathway.[27,52] In the free-energy pathways (Figure 3C and 3D), the energetically most difficult step, or potential-determining step, corresponds to initial hydrogenation of adsorbed $N_2$* to form an NNH* intermediate. An onset potential of about 1.325 V is required to make all the NRR elementary steps downhill in terms of free energy on the pure $SnO_2$(110) surface. However, the potential-determining potential decreases to about 0.803 V on Fe–$SnO_2$(110). It indicates that the electrocatalytic activity of oxygen vacancy-anchored Fe atom in the NRR is higher than that of the surface under-coordinated Sn atom. The introduction of oxygen vacancy-anchored Fe enables an alternative NRR mechanism (Figure S38-39). For NOR, the most demanding step is the first-step oxidation of $N_2$ to form NN(OH)*, which has an endothermic free energy of 3.581 eV on $SnO_2$(110) and 2.585 eV on Fe–$SnO_2$(110) (Figure 3E, 3F and S40-41). It suggests that the introduction of oxygen vacancy-anchored Fe can increase the electrocatalytic efficiency for both $N_2$ reduction and oxidation. The electronic structures of $SnO_2$ and lattice Fe doped $SnO_2$ were also explored. Figure S42-S44 showed the calculated density of states (DOS) of $SnO_2$, lattice Fe doped $SnO_2$ and oxygen vacancy-anchored Fe in Fe–$SnO_2$ slab by DFT methods. Compared with $SnO_2$, lattice Fe doped $SnO_2$ exhibited a defect level below the conduction band, which effectively narrowed the band gap and enhanced the electrical conductivity. It could also be confirmed by the electrochemical impedance spectroscopy (EIS) spectra in NRR (Figure S45). In the Nyquist plots, a smaller charge transfer resistance ($R_{ct}$) was obatined for Fe-$SnO_2$ under exact same conditions. Therefore, it is reasonable that the oxygen vacancy-anchored Fe in Fe–$SnO_2$ act as the active site and the lattice doped Fe answers for the improved electrical conductivity, which are responsible for the enhanced $N_2$ fixation performance together.

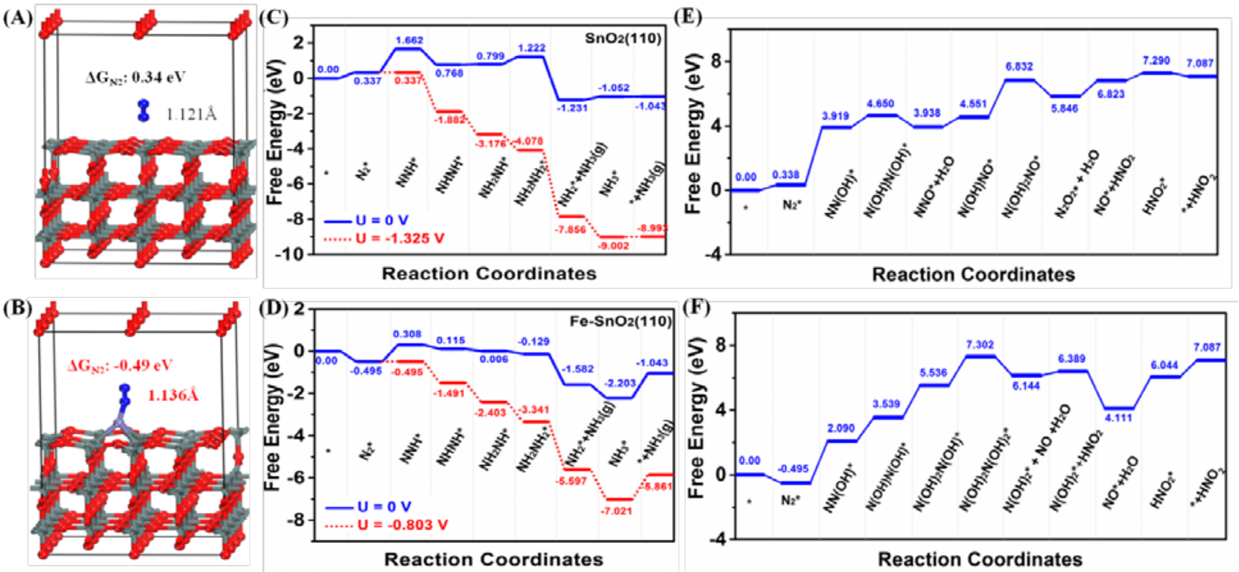

**Figure 3.** Stable adsorption configurations and corresponding adsorption energies for $N_2$* on hydrogenated (110) surface of $SnO_2$ (A) and surface-anchored Fe (B) in Fe–$SnO_2$ model; blue (N), gray (Sn), red (O), purple (Fe). (C) Free energy diagram of the NRR pathway along the alternating mechanism over the Sn site of pure $SnO_2$ (110) surface in acid condition at U = 0 and U = -1.325 V, respectively; (D) Free energy diagram of the NRR pathway along the alternating mechanism over the Fe site of Fe-$SnO_2$ (110) in acid condition at U = 0 and U = -0.803 V, respectively. (E) Free-energy diagram for NOR under acidic conditions over the $SnO_2$(110) surface and (F) free-energy diagram for NOR under acidic condition over Fe-doped $SnO_2$(110) surface.

In summary, a new-type Fe–$SnO_2$ was synthesized and explored as an advanced electrocatalyst for ambient $N_2$ fixation. A remarkable large $NH_3$ yield of 82.7 μg $h^{-1}$ $mg_{cat.}^{-1}$ and a FE 20.4 % were obtained for NRR, superior than all the reported catalyst in acid electrolyte. Besides, a $NO_3^-$ yield of 42.9 μg $h^{-1}$ $mg_{cat.}^{-1}$ and a FE of 0.84% were also obtained for the Janus catalyst in acid electrolyte. The outstanding activity was ascribed to the improved adsorption and activation of $N_2$ and improved electrical conductivity for the co-existence of the oxygen vacancy-anchored Fe on $SnO_2$ and the lattice doped Fe. DFT calculations suggested the breakage of $N\equiv N$ was the energetically most difficult step for both NRR and NOR, the oxygen vacancy-anchored single-atom Fe can effectively adsorb and activate chemical inert $N_2$ molecules, lower the energy barrier, resulting in the enhanced $N_2$ fixation performance. This work offered a neoteric catalytic structure and provided brand new ideas for the rational design of electrocatalysts for artificial $N_2$ fixation.

## Acknowledgements ((optional))

This work was supported by the National Natural Science Foundation of China (21908120 and 21875030), the Natural Science Foundation of Shandong Province (ZR2018BB037), the Youth Innovation Team Project of Shandong Provincial Education Department (2019KJC023) and project of Qingdao Applied Basic Research Programs of Science and Technology (18-2-2-10-jch and 18-2-2-35-jch)

**Keywords:** $N_2$ fixation • electrochemical nitrogen reduction • electrochemical nitrogen oxidation • bifunctional

[1] B. H. R. Suryanto, H.-L. Du, D. Wang, J. Chen, A. N. Simonov, D. R. MacFarlane *Nat. Catal.* **2019**, *2*, 290-296.
[2] X. Cui, C. Tang, Q. Zhang *Adv. Energy Mater.* **2018**, *8*, 1800369.
[3] Y. Zhu, L. Peng, Z. Fang, C. Yan, X. Zhang, G. Yu *Adv. Mater.* **2018**, *30*, e1706347.
[4] Y. C. Wan, J. C. Xu, R. T. Lv *Mater. Today*. **2019**, *27*, 69-90.
[5] X. Zhu, T. Wu, L. Ji, C. Li, T. Wang, S. Wen, S. Gao, X. Shi, Y. Luo, Q. Peng, X. Sun *J. Mater. Chem. A*. **2019**, *7*, 16117-16121.
[6] M. Cheng, C. Xiao, Y. Xie *J. Mater. Chem. A*. **2019**, *7*, 19616-19633.
[7] Y. Wang, Y. Yu, R. Jia, C. Zhang, B. Zhang *Natl. Sci. Rev.* **2019**, *6*, 730-738.
[8] Y. Liu, M. Cheng, Z. He, B. Gu, C. Xiao, T. Zhou, Z. Guo, J. Liu, H. He, B. Ye, B. Pan, Y. Xie *Angew Chem. Int. Ed.* **2019**, *58*, 731-735.
[9] N. Cao, Z. Chen, K. Zang, J. Xu, J. Zhong, J. Luo, X. Xu, G. Zheng *Nat. Commun.* **2019**, *10*, 2877.
[10] R. Shi, Y. X. Zhao, G. I. N. Waterhouse, S. Zhang, T. R. Zhang *Acs Catal.* **2019**, *9*, 9739-9750
[11] L. Xia, B. Li, Y. Zhang, R. Zhang, L. Ji, H. Chen, G. Cui, H. Zheng, X. Sun, F. Xie, Q. Liu *Inorg. Chem.* **2019**, *58*, 2257-2260.
[12] M. Wang, S. Liu, T. Qian, J. Liu, J. Zhou, H. Ji, J. Xiong, J. Zhong, C. Yan *Nat. Commun.* **2019**, *10*, 341.
[13] H. Tao, C. Choi, L.-X. Ding, Z. Jiang, Z. Han, M. Jia, Q. Fan, Y. Gao, H. Wang, A. W. Robertson, S. Hong, Y. Jung, S. Liu, Z. Sun *Chem*. **2019**, *5*, 204-214.
[14] L. Xia, X. Wu, Y. Wang, Z. Niu, Q. Liu, T. Li, X. Shi, A. M. Asiri, X. Sun *Small Methods*. **2018**, *3*, 1800251.
[15] H. Cheng, L. X. Ding, G. F. Chen, L. Zhang, J. Xue, H. Wang *Adv. Mater.* **2018**, *30*, 1803694.
[16] T. Wu, X. Zhu, Z. Xing, S. Mou, C. Li, Y. Qiao, Q. Liu, Y. Luo, X. Shi, Y. Zhang, X. Sun *Angew Chem Int. Ed.* **2019**, *58*, 18449-18453.
[17] C. Li, J. Yu, L. Yang, J. Zhao, W. Kong, T. Wang, A. M. Asiri, Q. Li, X. Sun *Inorg. Chem.* **2019**, *58*, 9597-9601..
[18] Y. Li, Q. Zhang, C. Li, H.-N. Fan, W.-B. Luo, H.-K. Liu, S.-X. Dou *J. Mater. Chem. A*. **2019**, *7*, 22242-22247.
[19] X. Zhu, T. Wu, L. Ji, C. Li, T. Wang, S. Wen, S. Gao, X. Shi, Y. Luo, Q. Peng, X. Sun *J. Mater. Chem. A*. **2019**, *7*, 16117-16121.
[20] J. Wang, B. Huang, Y. Ji, M. Sun, T. Wu, R. Yin, X. Zhu, Y. Li, Q. Shao, X. Huang *Adv. Mater.* **2020**, e1907112.
[21] J. Li, S. Chen, F. Quan, G. Zhan, F. Jia, Z. Ai, L. Zhang *Chem*. **2020**.
[22] L. Xia, J. Yang, H. Wang, R. Zhao, H. Chen, W. Fang, A. M. Asiri, F. Xie, G. Cui, X. Sun *Chem. Commun.* **2019**, *55*, 3371-3374.
[23] C. Li, S. Mou, X. Zhu, F. Wang, Y. Wang, Y. Qiao, X. Shi, Y. Luo, B. Zheng, Q. Li, X. Sun *Chem. Commun.* **2019**, *55*, 14474-14477
[24] W. Luc, C. Collins, S. Wang, H. Xin, K. He, Y. Kang, F. Jiao *J. Am. Chem. Soc.* **2017**, *139*, 1885-1893.
[25] S. Liu, J. Xiao, X. F. Lu, J. Wang, X. Wang, X. W. D. Lou *Angew Chem. Int. Ed.* **2019**, *58*, 8499-8503.
[26] D. Gao, Y. Zhang, Z. Zhou, F. Cai, X. Zhao, W. Huang, Y. Li, J. Zhu, P. Liu, F. Yang, G. Wang, X. Bao *J. Am. Chem. Soc.* **2017**, *139*, 5652-5655.
[27] Y. P. Liu, Y. B. Li, H. Zhang, K. Chu *Inorg. Chem.* **2019**, *58*, 10424-10431.
[28] L. Zhang, X. Ren, Y. Luo, X. Shi, A. M. Asiri, T. Li, X. Sun *Chem. Commun.* **2018**, *54*, 12966-12969.
[29] Y. Chen, L. Liu, Y. Peng, P. Chen, Y. Luo, J. Qu *J. Am. Chem. Soc.* **2011**, *133*, 1147-1149.
[30] Y. Li, Y. Li, B. Wang, Y. Luo, D. Yang, P. Tong, J. Zhao, L. Luo, Y. Zhou, S. Chen, F. Cheng, J. Qu *Nat. Chem.* **2013**, *5*, 320-326.
[31] X. Zhu, Z. Liu, H. Wang, R. Zhao, H. Chen, T. Wang, F. Wang, Y. Luo, Y. Wu, X. Sun *Chem. Commun.* **2019**, *55*, 3987-3990.
[32] H. Huang, F. Li, Q. Xue, Y. Zhang, S. Yin, Y. Chen *Small*. **2019**, *15*, 1903500.
[33] X. Cui, C. Tang, X. M. Liu, C. Wang, W. Ma, Q. Zhang *Chemistry*. **2018**, *24*, 18494-18501.
[34] Q. Liu, X. Zhang, B. Zhang, Y. Luo, G. Cui, F. Xie, X. Sun *Nanoscale*. **2018**, *10*, 14386-14389.
[35] Y. Li, Y. Kong, Y. Hou, B. Yang, Z. Li, L. Lei, Z. Wen *ACS Sustain. Chem. Eng.* **2019**, *7*, 8853-8859.
[36] X. Zhu, Z. Liu, Q. Liu, Y. Luo, X. Shi, A. M. Asiri, Y. Wu, X. Sun *Chem. Commun.* **2018**, *54*, 11332-11335.
[37] X. Zhao, X. Lan, D. Yu, H. Fu, Z. Liu, T. Mu *Chem. Commun.* **2018**, *54*, 13010-13013.
[38] L. Xia, J. Yang, H. Wang, R. Zhao, H. Chen, W. Fang, A. M. Asiri, F. Xie, G. Cui, X. Sun *Chem. Commun.* **2019**, *55*, 3371-3374.
[39] X. Liu, H. Jang, P. Li, J. Wang, Q. Qin, M. G. Kim, G. Li, J. Cho *Angew Chem. Int. Ed.* . **2019**, *58*, 13329-13334.
[40] X. Qu, L. Shen, Y. Mao, J. Lin, Y. Li, G. Li, Y. Zhang, Y. Jiang, S. Sun *ACS Appl. Mater. Inter.* **2019**, *11*, 31869-31877.
[41] W. Qiu, X. Y. Xie, J. Qiu, W. H. Fang, R. Liang, X. Ren, X. Ji, G. Cui, A. M. Asiri, G. Cui, B. Tang, X. Sun *Nat. Commun.* **2018**, *9*, 3485.
[42] C. Lv, Y. Qian, C. Yan, Y. Ding, Y. Liu, G. Chen, G. Yu *Angew Chem. Int. Ed.* **2018**, *57*, 10246-10250.
[43] F. Xu, L. Zhang, X. Ding, M. Cong, Y. Jin, L. Chen, Y. Gao *Chem. Commun.* **2019**, *55*, 14111-14114
[44] C. D. Lv, C. S. Yan, G. Chen, Y. Ding, J. X. Sun, Y. S. Zhou, G. H. Yu *Angew Chem Inte. Ed.* **2018**, *57*, 6073-6076.
[45] Y. Chen, S. Ji, C. Chen, Q. Peng, D. Wang, Y. Li *Joule*. **2018**, *2*, 1242-1264.
[46] J. Wan, W. Chen, C. Jia, L. Zheng, J. Dong, X. Zheng, Y. Wang, W. Yan, C. Chen, Q. Peng, D. Wang, Y. Li *Adv. Mater.* **2018**, *30*.
[47] H. Li, S. Wang, H. Sawada, G. G. Han, T. Samuels, C. S. Allen, A. I. Kirkland, J. C. Grossman, J. H. Warner *ACS Nano*. **2017**, *11*, 3392-3403.
[48] S. Zhang, P. N. Plessow, J. J. Willis, S. Dai, M. Xu, G. W. Graham, M. Cargnello, F. Abild-Pedersen, X. Pan *Nano Lett.* **2016**, *16*, 4528-4534.
[49] G. Liu, A. W. Robertson, M. M. Li, W. C. H. Kuo, M. T. Darby, M. H. Muhieddine, Y. C. Lin, K. Suenaga, M. Stamatakis, J. H. Warner, S. C. E. Tsang *Nat. Chem.* **2017**, *9*, 810-816.
[50] A. Sasahara, C. L. Pang, H. Onishi *J. Phys. Chem. B*. **2006**, *110*, 13453-13457.
[51] Y. Tong, H. Guo, D. Liu, X. Yan, P. Su, J. Liang, S. Zhou, J. Liu, G. Q. M. Lu, S. X. Dou *Angew Chem. Int. Ed.* **2020**. 10.1002/anie.202002029
[52] T. Wu, W. Kong, Y. Zhang, Z. Xing, J. Zhao, T. Wang, X. Shi, Y. Luo, X. Sun *Small Methods*. **2019**, *3*, 1900356.

# COMMUNICATION

A new-type Fe–$SnO_2$ was synthesized and explored as a Janus electrocatalyst for both NRR and NOR firstly. The Fe elements in Fe–$SnO_2$ can be categorized into oxygen vacancy anchored Fe and lattice doped Fe, which enhances the adsorption and activation of $N_2$ on $SnO_2$ and improves the electrical conductivity of $SnO_2$, respectively. As a consequence, the catalyst exhibited excellent catalytic performance toward both NRR and NOR: a high $NH_3$ yield of 82.7 µg $h^{-1}$ $mg_{cat.}^{-1}$ and a FE of 20.4% and a high $NO_3^-$ yields of 42.9 µg $h^{-1}$ $mg_{cat.}^{-1}$ and a FE of 0.84% .

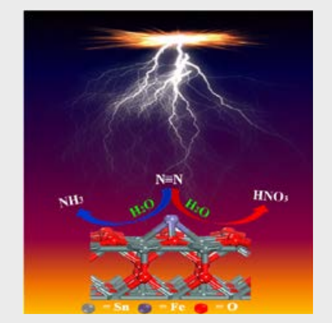

*Linlin Zhang, Meiyu Cong, Xin Ding*, Yu Jin, Yong Wang, Fanfan Xu, Lin Chen, Lixue Zhang**

***Page No. 1– Page No.5***

**A Janus Fe-$SnO_2$ Catalyst Enables Bifunctional Electrochemical Nitrogen Fixation**